School of Biomedical Engineering, Science, and Health Systems

Atlas-Based Indexing of Brain Sections via 2-D to 3-D Image Registration

Smadar Gefen*, *Member, IEEE*, Nahum Kiryati, *Senior Member, IEEE*, and Jonathan Nissanov, *Member, IEEE*

***Abstract*—A 2-D to 3-D nonlinear intensity-based registration method is proposed in which the alignment of histological brain sections with a volumetric brain atlas is performed. First, sparsely cut brain sections were linearly matched with an oblique slice automatically extracted from the atlas. Second, a planar-to-curved surface alignment was employed in order to match each section with its corresponding image overlaid on a curved-surface within the atlas. For the latter, a PDE-based registration technique was developed that is driven by a local normalized-mutual-information similarity measure. We demonstrate the method and evaluate its performance with simulated and real data experiments. An atlas-guided segmentation of mouse brains' hippocampal complex, retrieved from the Mouse Brain Library (MBL) database, is demonstrated with the proposed algorithm.**

***Index Terms*—Normalized mutual information, PDE-based methods, 2-D to 3-D nonlinear registration.**

I. Introduction

In RECENT years, numerous approaches for 2-D to 2-D and 3-D to 3-D image registration have been studied. Several comprehensive surveys of image registration have been published summarizing the research on this important topic [1]–[8]. Many of these registration algorithms dealt with images that had the same resolution, dimension, and support. However, dealing with nonisotropic, unevenly sampled, not equal-dimensional, or incomplete datasets remains a challenge. This challenge is especially pertinent to biomedicine where volumetric images from various modalities are often reconstructed from previously acquired sectional images.

A. Background

In the literature, 2-D to 3-D alignment methods are often proposed in the context of aligning 3-D data to their projective images in order to solve a 3-D model pose problem. An example of such an alignment is the spatial mapping between the 3-D model of an object and the coordinate system of a physical scene. In image-guided surgery, 2-D to 3-D registration is used to map a preoperative segmented 3-D model of an organ to the operating room coordinate system. For instance, intracranial aneurysms are treated via endovascular coiling: A micro-catheter is image-guided through a small puncture in the femoral artery up into the cerebral artery in the location of the aneurysm to be treated. In this application 3-D magnetic resonance angiography (MRA) is registered with 2-D X-ray angiograms using either an intensity-based method [9]–[11] or feature-based method [12]–[14]. Another example is localizing the center of a tumor in the liver which is to be treated with radio frequency. In this case, tumor center localization is achieved via registration of a 3-D CT image of the liver with 2-D video images [15].

Most of the studies dealing with 2-D to 3-D registration techniques were confined to rigid-body transformation [16]–[19]. Kim *et al.* [16], for instance, performed motion correction by mapping each slice of functional magnetic resonance imaging (fMRI) image onto the volumetric MR image which was acquired in the same session by using a rigid-body transformation. However, anatomical changes over time, patients' movements, or limitations of the imaging procedure may create nonlinear deformation and, therefore, require a method that will compensate for that.

Nonrigid registration of postmortem brain slices to MRI volume was proposed by Kim *et al.* [20], where a polynomial transformation was used to parametrically represent the deformation field. Slice-to-volume nonlinear registration was also proposed by Liu *et al.* [21] for the application of ultrasound spatial compounding. In [21], cubic B-spline functions were used to approximate the deformation field based on given control points. In contrast, in this study, we propose an image-based registration method (no corresponding points are required) that restores a free-form deformation field relating histological sections from experimental dataset to histological volumetric atlas of mouse brains. This operation facilitates indexing of sections of interest by the Atlas.

B. Atlas-Based Indexing of Mouse Brain Sections

Histological images of mouse brains allow detailed structural analysis and have been critical to our present understanding of the nervous system. They are generated by cutting the brains into thin slices (sections) that are then stained to demarcate specific tissue types or localized particular chemical moieties. The tissue slices are then imaged with a scanner or a microscope, yielding a set of 2-D ordered but unaligned images. Often, not every tissue section is collected and the data sets have a much

Manuscript received March 21, 2006; revised March 19, 2007. This work was supported in part by the Human Brain Project under Grant P20 MH62009 and in part by the National Science Foundation under DBI Grant 0352421. *Asterisk indicates corresponding author*.

*S. Gefen is with PVI Virtual Media Services LLC, 15 Princess Road, Lawrenceville, NJ 08648 USA (e-mail: sgefen@pvi.tv).

N. Kiryati is with the Electrical Engineering School, Tel-Aviv University, Ramat Aviv 69978, Israel (e-mail: nk@eng.tau.ac.il).

J. Nissanov is with the Laboratory for Bioimaging and Anatomical Informatics, Department of Neurobiology and Anatomy, Drexel University College of Medicine, Philadelphia, PA 19129-1096 USA (e-mail: jonathan.nissanov@drexelmed.edu).

Color versions of one or more of the figures in this paper are available online at http://ieeexplore.ieee.org.

Digital Object Identifier 10.1109/TBME.2007.899361

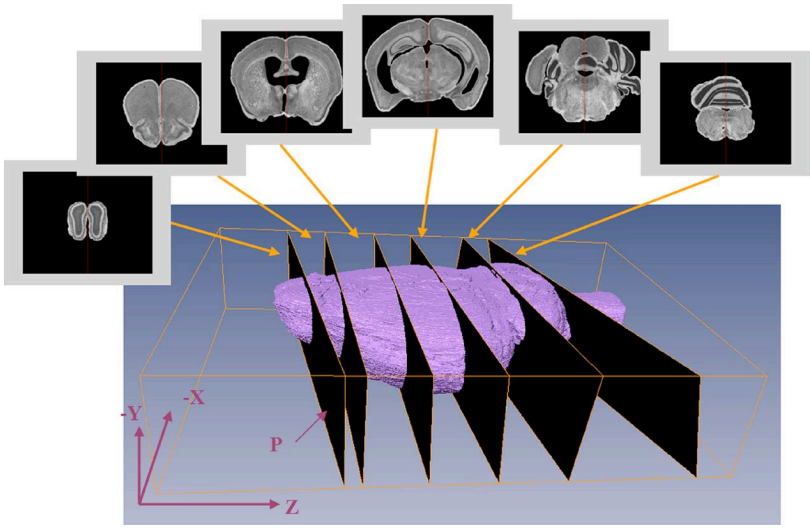

Fig. 1. Localization of brain images from the MBL database (2-D monochromatic views) on the 3-D atlas. Each image is matched with the planar-surface within the atlas that best corresponds to it. Typically, each brain in the MBL is composed of 30 horizontal or 70 coronal sections with 150-μm intersection spacing.

higher in-plane resolution than out-of-plane (intersection) resolutions.

Our focus on mice is due to its importance in modern biomedical research. Mice have come to be the mammal of choice in genetic research. The mouse brain is small ($\sim 1 \times 0.5 \times 2$ cm) and is readily available. In addition to its value as a model of human neurobiological and neuropathological processes, it is useful as a test bed to advance image analysis technologies that are applicable directly to larger human brain images.

Neuroscience research, and, in particular, where mice serve as a model system, is in critical need of effective spatial normalization methods that permit combining data derived from different specimens [22]. This is particularly the case in discovery-based methods where large image databases, such as GENSAT (http://www.ncbi.nlm.nih.gov/projects/gensat), the Allen Brain Atlas (http://www.brainatlas.org), and our own Mouse Brain Library (http://www.mbl.org), are being created to support a wide range of research projects. Spatial normalization could allow large scale automated mining of the datasets by supporting voxel-by-voxel comparison of aligned brain images and automated segmentation of this data using canonical aligned annotation templates.

The Mouse Brain Library (MBL) is a database of approximately 200 000 coronal and horizontal (axial) histological images representing about 4000 mice from over 120 strains [22]. The library was developed to assist in a type of genetic mapping, known as complex trait analysis, where phenotypic variations (in this case anatomical) are correlated to genotypic variations between mice strains. The objective of the present study is to develop a method to align each section from this database to its corresponding surface within a canonical 3-D atlas, as illustrated in Fig. 1. A particular challenge in registration of MBL, and for that matter, of most histological datasets from animal research, is the sparse section collection strategies employed. In the case of MBL, every fifth 30-μm-thick section is collected (a section every 150 μm). Our approach overcomes this difficuly and consists of two stages. First a linear match is found for each brain section with a planar-surface within the atlas that best corresponds to it and then the alignment is refined by matching each section to the corresponding image on a curved surface. This alignment facilitates automatic atlas-guided segmentation.

C. Level-Set-Based Approach to Image Registration

Level-set-based methods, pioneered by Osher and Sethian [23], have been intensively studied mainly in the context of segmentation and tracking of deformable objects [24]–[26]. Briefly, level-set is an implicit representation of a surface. It is defined by a scalar function $\phi(\mathbf{x}) : R^3 \rightarrow R$, such that a surface S is determined by a scalar k as follows: $S = \{\mathbf{x} | \phi(\mathbf{x}) = k\}$. This level-set formulation provides the mechanism for a family of PDE-based methods that are solved numerically on a grid and that control the deformation of S via changing the scalar values of $\phi(\mathbf{x})$.

The deformation of the surface S is controlled by the evolution equation

$$\frac{\partial \phi(\mathbf{x}, t)}{\partial t} + V(\mathbf{x}) \left| \nabla \phi(\mathbf{x}, t) \right| = 0 \tag{1}$$

where $V(\mathbf{x})$ is the spatial speed at the direction of the surface normal $\mathbf{n}(\mathbf{x}) = \nabla \phi(\mathbf{x}, t) / \left\| \nabla \phi(\mathbf{x}, t) \right\|$ at a point $\mathbf{x}$ [23]. The speed function is designed to control the surface evolution based on intrinsic properties (e.g., curvature) and/or extrinsic properties (e.g., image gradient).

Recently, Vemuri *et al.* [27] proposed using the level-set curve evolution technique for image registration. The level-set function $\phi(\mathbf{x})$ was replaced by the image $I_1(\mathbf{x}) : R^3 \rightarrow R$, defined in a domain $\Omega \in R^3$, where its gray-scale values constitute the level-sets. Thus, this registration method involves the evolution of $I_1(\mathbf{x})$ toward a destination image $I_2(\mathbf{x})$ in the direction of the iso-surfaces' normals and with a speed that is a function of the distance between $I_1(\mathbf{x})$ and $I_2(\mathbf{x})$

$$\frac{\partial I(\mathbf{x}, t)}{\partial t} + (I_2(\mathbf{x}) - I(\mathbf{x}, t)) \left| \nabla I(\mathbf{x}, t) \right| = 0 \tag{2}$$

where $I(\mathbf{x}, 0) = I_1(\mathbf{x})$.

The equation above morphs the image $I_1(\mathbf{x})$ to match the image $I_2(\mathbf{x})$, but it does not provide the deformation field $\mathbf{u}(\mathbf{x}) : R^3 \rightarrow R^3$ that maps $I_1(\mathbf{x})$ to $I_2(\mathbf{x}) : I_1(x-u, y-v, z-w) = I_2(x, y, z)$. Explicitly having the displacement field is essential in most registration applications, if only to enable registration validation. Hence, an alternative equation was suggested in [27]

$$\frac{\partial \mathbf{u}(\mathbf{x}, t)}{\partial t} + (I_2(\mathbf{x}) - I_1(\mathbf{x} - \mathbf{u}(\mathbf{x}, t))) \frac{\nabla I_1(\mathbf{x} - \mathbf{u}(\mathbf{x}, t))}{|\nabla I_1(\mathbf{x} - \mathbf{u}(\mathbf{x}, t))|} = 0. \tag{3}$$

The evolution equation (3) is designed to recover the deformation field between homologous images created by the same modality, i.e., assuming corresponding regions are with the same voxel intensity values. Vemuri *et al.* [27] demonstrated this method in the application of atlas-guided segmentation through 3-D to 3-D registration of MRI images. Registration of images from different modalities, however, requires a different formulation of the speed function $V(\mathbf{x})$.

In this study, we first incorporate the PDE in (3) into a 2-D to 3-D registration framework. Second, we propose a new evolution equation that uses local normalized mutual information (NMI) measure to drive the image evolution. Local mutual information (MI) was proposed by Hermosillo [28] to drive a nonrigid 2-D image registration. In [28], a Parzen estimator was used for the joint probability and MI similarity measure was maximized using a variational framework. In our approach, 3-D image registration is achieved by computing numerically both the joint probability (based on a 2-D histogram) and the local NMI gradient. Thus, the deformation field evolves in a direction that maximizes the NMI similarity measure.

This study expands on and further validates a preliminary study where a piecewise linear registration method [29] and a nonlinear registration method [30] were explored. In this study we present a full solution for the indexing of a large database of brain sections with a volumetric atlas. The rest of the paper is organized as follows. In Section II, the proposed algorithm for atlas-based indexing is described, Section III presents simulations and real data experiments in which the hippocampus of a mouse brain is segmented, and we conclude with a discussion in Section IV.

II. Algorithm Description

The proposed 2-D to 3-D image registration method was motivated by the application of atlas-based indexing of brain sections from the MBL database. Hence, given a subset of sparse sectional data of a brain, the objective was to find for each section (2-D image) the corresponding image on a curved-surface within the atlas (3-D image). This task was carried out in two steps. First, we employed an affine mapping in which each section was matched with an image on a plane P within the atlas volume that best explains it. Second, the corresponding image on a curved-surface, defined in the vicinity of the corresponding plane P, was recovered. The image to planar surface matching stage is described in subsection A and the image to curved-surface matching stage is described in subsection B.

A. Image to Planar Surface Matching (IPSM)

The following is the description of a registration method that finds the planar-surface within a volumetric image for which its overlaid image best matches a given brain section image. This image-to-planar surface-matching method is referred to here as IPSM. In the IPSM method, each given section image, $I_s(\mathbf{x})$, is paired with the best matching image on a plane P within the atlas volume. Since intersubject variability is 3-D, pursuing the matching plane is merely an approximation and is done as an initialization stage for the next nonrigid stage of planar to curved-surface image matching.

Consider the coordinate system shown in Fig. 2. A plane P is a quasi-coronal plane within the atlas volume $I_v : R^3 \rightarrow R$ and can be defined by its crossing point with the axis: $z = z_0$, and its rotation angles α_x and α_y with respect to the x and y axes, respectively. Alternatively, P can be defined by the plane equation $\{x \in P | ax + by + c(z - z_0) = 0\}$, where $a = -\tan(\alpha_y)$ and $b = -\tan(\alpha_x)/\cos(\alpha_y)$ and c $= 1$. Thus, $I_p : R^2 \rightarrow R$, the 2-D image overlaid on the plane P, can be defined as $I_p = I_v(\mathbf{x}) : \mathbf{x} \in P$. Note that, although the illustration in Fig. 1 shows quasi-coronal sections, the same argument can be made for registration of quasi-horizontal or quasi-sagittal sections to the atlas.

In general, given a quasi-coronal section, one needs to initialize the IPSM algorithm with an estimate for its location z_0 within the atlas. Usually, this estimate is readily available since the region of interest is known. In our case, each MBL section is given as part of a sparse set of sections from one brain, thereby initializing the IPSM algorithm is performed as follows. The registration of a section, $I_s = I_s^i$, onto its corresponding planar image in the atlas, I_p, is carried out starting with the normalization of the atlas, I_v, with the MBL brain, $\left\{I_s^i(\mathbf{x}) : R^2 \rightarrow R | i = 1 \ldots N\right\}$, based on a subset of points from their external surfaces. This is done with a 3-D surface-based affine registration algorithm described in [31]. At this point, each given section I_s is positioned in the vicinity of its matching planar-image, I_p, within the atlas. Next, a search is employed to find the best plane P that in turn results in the best matching I_p to I_s.

Although both the given dataset and the atlas are histological images, the intensity and texture of corresponding regions are not similar due to intrinsic differences between animals as well as differences in tissue preparation methods. Hence, we chose to use NMI as the registration similarity measure. NMI, proposed by Studholme *et al.* [32], is invariant to the degree of overlap between images and was successfully used in numerous studies [5]. The NMI measures the statistical dependency of overlapping regions of two images as follows:

$$NMI(I_1, I_2) = \frac{H(I_1) + H(I_2)}{H(I_1, I_2)} \tag{4}$$

where $H(I_1) = -\sum_{n \in I_1} p(n) \log p(n)$ and $H(I_1, I_2) = -\sum_{n \in I_1} \sum_{m \in I_2} p(n, m) \log p(n, m)$ are the marginal and joint entropy, respectively. n and m denote random variables that take the intensity values of overlapping pixels from I_1 and I_2, respectively. A 2-D histogram, constructed by counting the

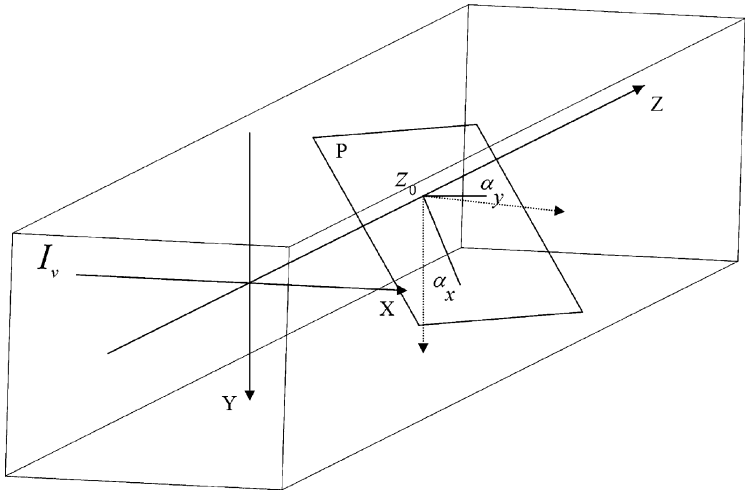

Fig. 2. Plane P is a quasi-coronal plane within the atlas volume I_v and can be viewed as a perpendicular plane to the Z axis, located at $z = z_0$, that go first thorough rotation α_x with respect to the x axis and then go through rotation α_y with respect to the y axis. Points on this plane follows the plane equation $\{x \in P | ax + by + c(z - z_0) = 0\}$, where $a = -\tan(\alpha_y)$ and $b = -\tan(\alpha_x)/\cos(\alpha_y)$ and $\mathrm{c} = 1$.

population of overlapping pixels' intensities, is used to estimate the joint and marginal probabilities.

Next, the registration parameters that define a corresponding image I_p are computed. This is done through maximization of the NMI similarity metric

$$\boldsymbol{\theta} = \arg(\max_{\boldsymbol{\theta}} NMI(\mathbf{I}^i_{ms}(\mathbf{x}; \mathbf{R}, \mathbf{d}), I_p(\mathbf{x}, \boldsymbol{\pi})) \tag{5}$$

where $\mathbf{x} \in R^2$ is over the image I_p domain. The vector $\boldsymbol{\theta} \equiv [\boldsymbol{\pi}, \mathbf{R}, \mathbf{d}]$ contains the registration parameters. The $\boldsymbol{\pi} = [\alpha_x, \alpha_y, z_0]$ parameter vector defines the plane P within the atlas volume. The matrix $\mathbf{R} = [R_{11}, R_{12}, R_{21}, R_{22}]$ and the displacement vector $\mathbf{d} = [d_1, d_2]$ define the affine transformation that maps I^i_s onto I_p, hence, $I^i_{ms}(\mathbf{x}; \mathbf{R}, \mathbf{d}) = I^i_s(\mathbf{R}\mathbf{x} + \mathbf{d})$. Therefore, we search for the 2-D affine transformation that when applied to I^i_s will result in a matching image to the extracted atlas image (the atlas image overlaid on a plane defined by the parameters in $\boldsymbol{\pi}$). To carry out this matching both images, I^i_{ms} and I_p, are linearly interpolated.

In [29], it was shown that a global optimization method should be employed in order to locate the global maximum in (5). Nevertheless, many global optimization algorithms have been developed which are problem dependent [33]. Genetic algorithms (GAs)—a derivative free optimization method—have also been successfully applied to a large variety of global optimization problems [34]. Hence, we used a GA as our search engine as described in detail in [29].

B. Image-to-Curved Surface Matching (ICSM)

Once a matching image I_p to I_{ms} is found, the algorithm further refines the alignment by searching for a better matching image on a curved-surface in the vicinity of the plane P. To do this, the atlas volume is deformed according to a 3-D displacement field such that the voxels overlay the plane P resulting in a new image I'_p. Thus, the algorithm computes the displacement field that maximizes a local 3-D similarity metric between two volumes: 1) the atlas volume and 2) a volume which is an extension of the I_{ms} image and constructed as follows.

The image I_{ms} is first mapped onto the plane P and then extended into a volume as follows:

$$I_{\mathrm{ems}}(\mathbf{x}) \equiv I_{ms}(\mathbf{x}') \tag{6}$$

where $\mathbf{x}'$ is the closest point to $\mathbf{x}$ on P

$$\mathbf{x}' = \mathbf{x} - \mathrm{dist}(\mathbf{x}, \mathrm{P}) \frac{[\mathrm{a}, \mathrm{b}, \mathrm{c}]}{\sqrt{\mathrm{a}^2 + \mathrm{b}^2 + \mathrm{c}^2}} \tag{7}$$

and $\mathrm{dist}(\mathbf{x}, P)$ is the minimal Euclidean distance from $\mathbf{x}$ to P

$$\mathrm{dist}(\mathbf{x}, P) = \frac{(ax + by + c(z - z_0))}{\sqrt{a^2 + b^2 + c^2}}. \tag{8}$$

This extension allows us to relate information from 3-D blocks in I_v and I_{ems} and thereby recover deformation in an off-plane direction as well as in an in-plane direction.

The next step recovers the deformation field $\mathbf{u}(\mathbf{x})$ that relates the atlas volume, I_v, to the volume $I_{\mathrm{ems}}(\mathbf{X})$, as follows:

$$I_{\mathrm{ems}}(\mathbf{x}) = I_v(\mathbf{x} - \mathbf{u}(\mathbf{x})). \tag{9}$$

Note that, although $\mathbf{u}(\mathbf{x})$ is defined throughout the volume's support, the computation focuses only at the vicinity of the plane P.

Using the evolution equation in (3), restoring $\mathbf{u}(\mathbf{x})$ is done iteratively as follows:

$$\begin{aligned} \mathbf{u}(\mathbf{x}, t) = {} & \mathbf{u}(\mathbf{x}, t-1) - \Delta t \\ & \cdot (I_{\mathrm{ems}}(\mathbf{x}) - I_v(\mathbf{x} - \mathbf{u}(\mathbf{x}, t-1)) \\ & \cdot \frac{\nabla(G^\sigma_{3D} * I_v(\mathbf{x} - \mathbf{u}(\mathbf{x}, t-1)))}{||\nabla(G^\sigma_{3D} * I_v(\mathbf{x} - \mathbf{u}(\mathbf{x}, t-1)))|| + \alpha} \end{aligned} \tag{10}$$

$$\mathbf{u}_{[\alpha_x, \alpha_y, z_0]}(t) = Q(\mathbf{u}(x, t)) \tag{11}$$

$$\tilde{\mathbf{u}}_{[\alpha_x, \alpha_y, z_0]}(t) = \mathbf{u}_{[\alpha_x, \alpha_y, z_0]}(t) * G^\sigma_{2D} \tag{12}$$

$$\mathbf{u}(\mathbf{x}, t) = T(\tilde{\mathbf{u}}_{[\alpha_x, \alpha_y, z_0]}(t)) \tag{13}$$

where G^σ_{2D} and G^σ_{3D} are the 2-D and 3-D Gaussian kernels, respectively, with a standard deviation σ, and $*$ is the convolution operator. We used $\sigma = 1.0$ in all our experiments. The gradient operator ∇ is implemented with a central differencing.

A stabilization factor $\alpha = 0.1$ is added to stabilize the computation where $\|\nabla(G_{3D}^{\sigma} * I_v(\mathbf{x} - \mathbf{u}(\mathbf{x}, t-1)))\| \approx 0$. The operator Q extracts a planar image from a volume at location $[\alpha_x, \alpha_y, z_0]$. The operator T maps an image onto a plane located at $[\alpha_x, \alpha_y, z_0]$ within a volume, and then extends this planar image to fill in the rest of the volume according to (6). Note that regularization is achieved in two ways: with the Gaussian smoothing of the displacement field throughout the plane P in (11)–(13) after each iteration of (10), and with the multilevel implementation of the ICSM algorithm that restores the deformation in a coarse-to-fine fashion.

Using the evolution (10) to restore the deformation field, $\mathbf{u}(\mathbf{x})$, is not suitable when comparing brain images from different modalities or where voxel intensities of corresponding regions do not correlate. In this case, we propose to use an alternative evolution equation to (10) that is driven by the following speed function:

$$\begin{aligned} &V(\mathbf{x},t;\mathbf{d\delta}) \\ &= \frac{1}{2\mathbf{d\delta}}(NMI(\beta_{\mathbf{x},\mathbf{w}}(\tilde{\mathbf{x}})I_{\text{ems}}(\tilde{\mathbf{x}}), \beta_{\mathbf{x},\mathbf{w}}(\tilde{\mathbf{x}})I_v(\tilde{\mathbf{x}} - \mathbf{u}(\tilde{\mathbf{x}},t) + \mathbf{d\delta}) \\ &\quad - NMI(\beta_{\mathbf{x},\mathbf{w}}(\tilde{\mathbf{x}})I_{\text{ems}}(\tilde{\mathbf{x}}), \beta_{\mathbf{x},\mathbf{w}}(\tilde{\mathbf{x}})I_v(\tilde{\mathbf{x}} - \mathbf{u}(\tilde{\mathbf{x}},t) - \mathbf{d\delta})) \end{aligned} \tag{14}$$

where $\beta_{\mathbf{x},\mathbf{w}}(\tilde{\mathbf{x}})$ is a box function defined as

$$\beta_{\mathbf{x},\mathbf{w}}(\tilde{\mathbf{x}}) = \begin{cases} 1, & \begin{matrix} x - w_x < \tilde{x} < x + w_x \\ y - w_y < \tilde{y} < y + w_y \\ z - w_z < \tilde{z} < z + w_z \end{matrix} \\ 0, & \text{otherwise.} \end{cases}$$

$V(\mathbf{x}, t; \mathbf{d\delta})$ is a central differencing of the NMI measure. The NMI is computed locally and numerically within a box defined by $\beta_{\mathbf{x},\mathbf{w}}(\tilde{\mathbf{x}})$ according to (4). Note that $V(\mathbf{x}, t; \mathbf{d\delta})$ estimates the gradient of the NMI with respect to changes in the deformation field.

Given the above speed function the following evolution equation is proposed:

$$\begin{aligned} &\frac{\partial \mathbf{u}(\mathbf{x},t)}{\partial t} + V(\mathbf{x},t;\mathbf{d\delta}) \\ &\cdot \frac{\left(\left|\frac{\partial I_v(\mathbf{x}-\mathbf{u}(\mathbf{x},t))}{\partial x}\right|, \left|\frac{\partial I_v(\mathbf{x}-\mathbf{u}(\mathbf{x},t))}{\partial y}\right|, \left|\frac{\partial I_v(\mathbf{x}-\mathbf{u}(\mathbf{x},t))}{\partial z}\right|\right)}{\|\nabla I_v(\mathbf{x} - \mathbf{u}(\mathbf{x},t))\|} = 0. \end{aligned} \tag{15}$$

The PDE above evolves the deformation field $\mathbf{u}(\mathbf{x})$ in a direction that increases the NMI similarity measure. Comparing (15) with the level set evolution equation in (1), we see the analogy; where, in (1), the level set function, $\phi(\mathbf{x})$, is evolved in a direction normal to its iso-surfaces and with a speed $V(\mathbf{x})$, similarly, in (15), the evolution of the image $I_v(\mathbf{x})$ is carried out implicitly through the evolution of $\mathbf{u}(\mathbf{x}, t)$ that are done in a direction that increases the normalized mutual information.

The numerical discretization of (15) is shown in (16) found at the bottom of the page. Note that in image regions where $\nabla(I_v(\mathbf{x} - \mathbf{u}(\mathbf{x}, t)) \approx 0$, $\mathbf{u}(\mathbf{x})$ will not evolve through iterations. Thus, deformation recovery is done mainly in high gradient regions employing (16) and then this deformation is extrapolated into smooth regions employing (11)–(13).

The time step Δt in (10) and (16) is set such that the numerical stability of the solution is guaranteed. Stability is enforced following the Courant–Friedrichs–Levy (CFL) condition stating that the numerical wave speed $\Delta x/\Delta t$ should propagates at least as fast as the physical wave speed [26]. Thus, in our case, similarly to [27] and where $\Delta_x = 1$, the adaptive time step was obtained by

$$\Delta t = \eta \frac{1}{\max\limits_{(x,y,z)\in\Omega}\{|H_x| + |H_y| + |H_z|\}} \tag{17}$$

and

$$(\,H_x \quad H_y \quad H_z\,) = \frac{(\,E_x F_1 \quad E_y F_2 \quad E_z F_3\,)}{\|\nabla(G_{3D}^{\sigma} * I_v(\mathbf{x} - \mathbf{u}(\mathbf{x}, t-1)))\| + \alpha}$$

where $E \equiv G_{3D}^{\sigma} * I_v(\mathbf{x} - \mathbf{u}(\mathbf{x}, t-1))$ and with η empirically set to 0.5. $F_1 = F_2 = F_3 = (I_{\text{ems}}(\mathbf{x}) - I_v(\mathbf{x} - \mathbf{u}(\mathbf{x}, t-1))$ for the PDE in (10) and $(F_1, F_2, F_3) = (V(\mathbf{x}, t; d\delta_x), V(\mathbf{x}, t; d\delta_y), V(\mathbf{x}, t; d\delta_z))$ for the PDE in (16).

III. Experiments

The feasibility of the method described above was assessed through simulations and real data experiments. Histological images of mouse brains were used to demonstrate the performance of the algorithm. The atlas volumetric image and the given experimental brain sections were generated employing different procedures.

The atlas was generated as follows: a mouse brain was dissected, frozen and cut horizontally into 17.9-μm-thin sections using a low distortion cryosectioning method [35]. Sections were stained with cresyl violet and subsequently imaged with a pixel pitch of 8 μm. The reconstruction of the sections' images into a 3-D volume was done by aligning the sections onto their corresponding block-face images and then employing a section-to-section image-based rigid-body registration [36]. Finally, the aligned images were resampled to yield a 3-D $604 \times 320 \times 1104$ volume with an isotropic 17.9-μm voxel size [37].

The experimental brain sections from the MBL database were generated as follows: mouse brains were embedded in celloidin,

$$\begin{aligned} u(\mathbf{x},t) &= \frac{u(\mathbf{x},t-1) - \Delta t \cdot V(\mathbf{x},t-1;d\delta_x)\cdot|(G_{3D}^{\sigma} * I_v(\mathbf{x} - \mathbf{u}(\mathbf{x},t-1)))_x|}{\|\nabla(G_{3D}^{\sigma} * I_v(\mathbf{x} - \mathbf{u}(\mathbf{x},t-1)))\| + \alpha} \\ v(\mathbf{x},t) &= \frac{v(\mathbf{x},t-1) - \Delta t \cdot V(\mathbf{x},t-1;d\delta_y)\cdot|(G_{3D}^{\sigma} * I_v(\mathbf{x} - \mathbf{u}(\mathbf{x},t-1)))_y|}{\|\nabla(G_{3D}^{\sigma} * I_v(\mathbf{x} - \mathbf{u}(\mathbf{x},t-1)))\| + \alpha} \\ w(\mathbf{x},t) &= \frac{w(\mathbf{x},t-1) - \Delta t \cdot V(\mathbf{x},t-1;d\delta_z)\cdot|(G_{3D}^{\sigma} * I_v(\mathbf{x} - \mathbf{u}(\mathbf{x},t-1)))_z|}{\|\nabla(G_{3D}^{\sigma} * I_v(\mathbf{x} - \mathbf{u}(\mathbf{x},t-1)))\| + \alpha} \end{aligned} \tag{16}$$

TABLE I
IPSM ALGORITHM SEARCH ENGINE ACCURACY IN FINDING RANDOMLY SELECTED ATLAS PLANES. THE AVERAGE MEAN AND STANDARD DEVIATION OF THE ABSOLUTE DIFFERENCE ERROR, TAKEN ACROSS 30 TRIALS, ARE SHOWN AS A FUNCTION OF THE USED RESOLUTION LEVELS. THE ALGORITHM RUNNING TIMES ARE ALSO SHOWN, DEMONSTRATING THE TRADEOFF BETWEEN ACCURACY AND COMPLEXITY

	α_x		α_y		z_0		Time (minutes)
Resolution level	mean	std	mean	std	mean	std	
3	0.0092	0.0076	0.0056	0.0045	6.75	1.71	~0.35
2	0.0093	0.0084	0.0053	0.0050	3.64	1.34	~1.2
1	0.0076	0.0071	0.0040	0.0035	2.02	0.98	~4.15
0	0.0039	0.0039	0.0019	0.0022	0.49	0.55	~16

cut coronally into 30-μm sections, stained with cresyl violet, and then imaged with an in-plane resolution of 4.4 μm [38]. The two different tissue preparation methods employed for the atlas production and MBL dataset generation resulted in geometric and intensity differences between the atlas and the experimental brain sections. Celloidin embedding, in contrast to fresh frozen cryosectioning, yields wonderfully well-preserved microstructures but introduces global shrinkage. The combination of shrinkage and the thicker section collection protocol for the experimental sections resulted in more intense cresyl violet staining.

Both the IPSM and ICSM algorithms were carried out in a coarse-to-fine fashion. First, starting with a $604 \times 320 \times 1104$ pixel dimension of the atlas volume, $I_v(\mathbf{x})$, a four-level Laplacian pyramid was created [39]. Subsampling was preceded by a 3-D separable filtering of the image, setting the filter kernel to (0.05,0.25,0.4,0.25,0.05) according to certain constraints specified in [39]. Second, the registration parameters were restored starting at the lowest resolution level and proceeding to higher resolution levels. The registration parameters estimate of one level was used as an initial point for the next higher resolution level.

We first evaluated the accuracy of the IPSM algorithm's search engine. We randomly extracted 30 planes from the atlas, each defined by $\boldsymbol{\pi} = [\alpha_x, \alpha_y, z_0]$, and fed them into the IPSM algorithm. We set the GA searching window to ± 0.2 rad for $[\alpha_x, \alpha_y]$ and ± 32 pixels around an initial value for z_0 (assuming the true z_0 is within the searching window). Table I shows the average mean and standard deviation of the absolute difference error, taken across the 30 trials and as a function of the used resolution levels (100 iterations at each level). The improvement in accuracy is especially noticeable in the estimation of z_0.

Next, we tested the IPSM algorithm performance with real data. Given a section from the MBL library, we evaluated the algorithm feasibility to locate the corresponding atlas plane. We retrieved 30 coronal sections in the vicinity of the hippocampus complex, from randomly selected 30 MBL brains, and manually identified their corresponding arbitrarily oriented planes in the 3-D atlas using our own NeuroTerrain software [37]. This manual matching was done by an expert, five times for each section and on different days. We took the average of these five manual registration results as the "ground truth." Fig. 3 shows sample of MBL sections (center) localization employing the IPSM algorithm. The ground truth is shown on the left. The automatic MBL section localization achieved by the IPSM algorithm is shown on the right. Computing the average absolute difference between the ground truth values and the IPSM algorithm estimates for α_x, α_y, and z_0 yielded 0.077[rad], 0.016[rad], and 5.88[pixel], respectively, where the standard deviations were 0.042, 0.012, and 6.7, respectively. Computing the median of the absolute difference yielded 0.069[rad], 0.012[rad] and 3.64[pixel], respectively. For example, given that the atlas resolution is of 17.9 μm, the median of absolute difference for z_0 is equivalent to ~ 65 μm. Note that the variation of the expert matching results for z_0 is ~ 80 μm. This high variation reflects the existing normal high biological variation among specimens.

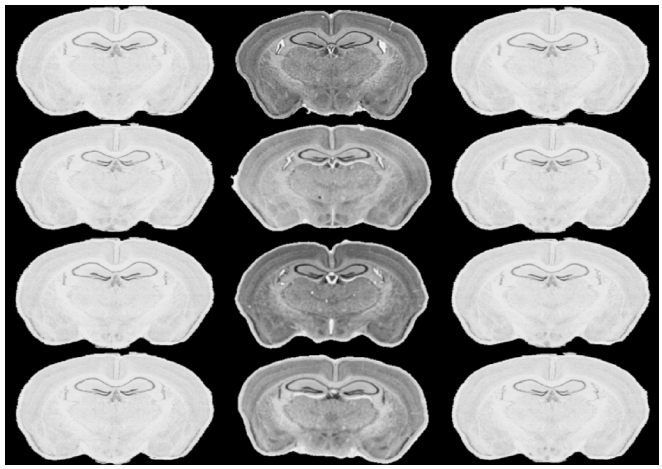

Fig. 3. Linear matching of MBL sections (center column) with planar images (left and right columns) extracted from the atlas. On the left column are shown matching results representing the ground truth (average of five manual registrations done by an expert). In the right column are shown matching results produced by the IPSM algorithm. Visual inspection shows that all results for matching planes are reasonably close to the given MBL section and can be used as a starting point for the nonlinear matching stage.

The ICSM algorithm's ability to match between an image and its corresponding image on a curved-surface was evaluated next. To carry out this test we created an elastic deformed version of the atlas $I_{test}(\mathbf{x}) = I_v(\mathbf{x} - U(\mathbf{x}))$, referred to here as the test volume. This was done using the thin-plate spline algorithm [41] with 27 pairs of corresponding points located on a 3-D grid. The vector distance between each pair of corresponding points was determined randomly within a range of ± 16 voxels [see Fig. 4(b) and (d)]. Next, to simulate a given MBL image, I_{ms}, we extracted sections from the test volume at 20 random positions $[\alpha_x, \alpha_y, z_0]$. Note that the displacement field that maps I_{ms} to its corresponding curved-surface within the atlas volume

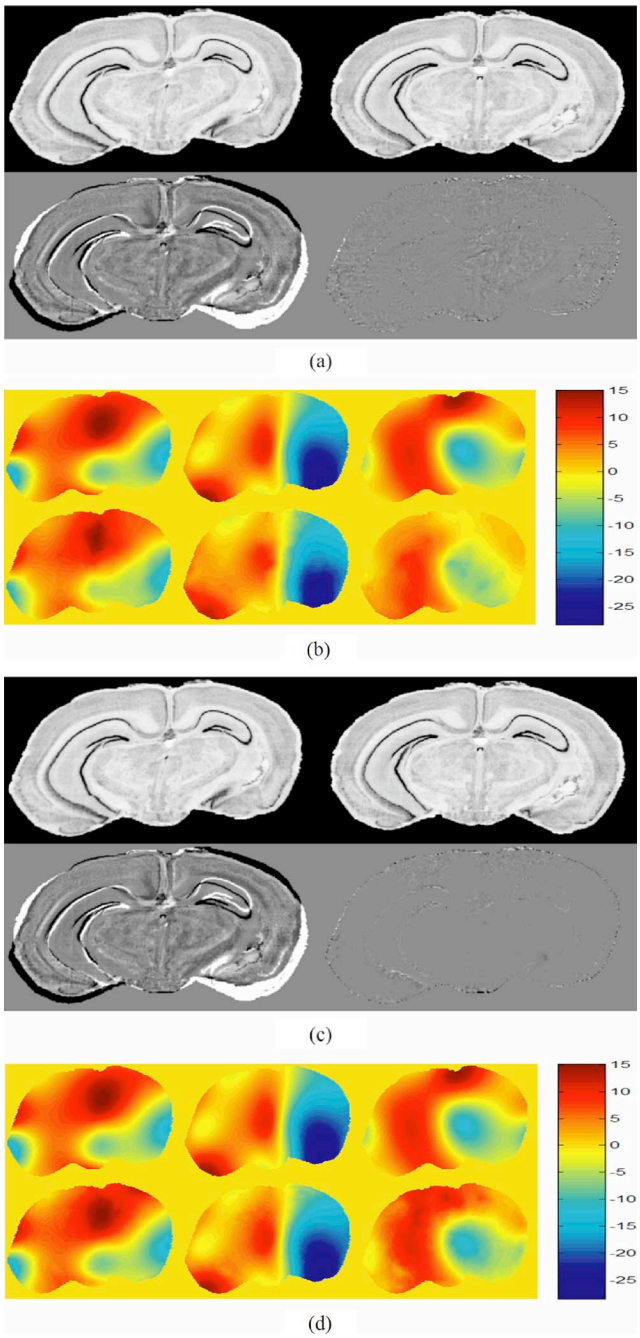

Fig. 4. Image-to-curved surface registration using a signed distance (a)–(b) and a normalized mutual information (c)–(d): in (a) and (c), the simulated image I_{ms} is shown on the top left along with the corresponding planar image I_p on the top right. Employing the ICSM algorithm a corresponding image on a curved- surface within the atlas, I'_p, was found. The difference image before registration, $I_{ms} - I_p + 127$ is shown on the bottom left and the difference image after registration, $I_{ms} - I'_p + 127$, is shown on the bottom right. In (b) and (d), the applied deformation $(U(\mathbf{x}), V(\mathbf{x}), W(\mathbf{x}))$ is shown on the top row and the estimated deformation $(u(\mathbf{x}), v(\mathbf{x}), w(\mathbf{x}))$ is shown on the bottom.

is known; hence, when employing the ICSM algorithm, the accuracy of the displacement field estimation could be evaluated.

The NMI measure in (14) was computed within a box defined by $(\mathrm{w}_x, \mathrm{w}_y, \mathrm{w}_z)$. This box dimension setting is a trade-off between the desired locality of the NMI measure and its statistical accuracy. Setting $(\mathrm{w}_x, \mathrm{w}_y, \mathrm{w}_z)$ to (4,4,1) resulted in an NMI computation within a $9 \times 9 \times 3$ box. The reason that w_z is smaller than $\mathrm{w}_x, \mathrm{w}_y$ is because most of the information in the given quasi-coronal section is in the x, y direction. Similarly, $(\mathrm{w}_x, \mathrm{w}_y, \mathrm{w}_z)$ is set to (1,4,4) and (4,1,4) when given quasi-saggital and quasi-horizontal sections, respectively. The histogram computation was done using a 32-bin size.

Fig. 4(a) and (b) shows the results for image-to-curve registration when using Vemuri's PDE in (10) and Fig. 4(c) and (d) shows the results when using the proposed PDE in (16). In Fig. 4(a) and (c), the simulated image I_{ms} is shown on the top-left along with the corresponding planar image I_p on the top right. Employing the ICSM algorithm, a corresponding image on a curved-surface within the atlas, I'_p, was found. The difference image before registration, $I_{ms} - I_p + 127$, is shown on the bottom-left and the difference image after registration, $I_{ms} - I'_p + 127$, is shown on the bottom-right. In Fig. 4(b) and (d), the applied deformation $\mathbf{U}(\mathbf{x}) = (U(\mathbf{x}), V(\mathbf{x}), W(\mathbf{x}))$ is shown on the top row and the estimated deformation $\mathbf{u}(\mathbf{x}) = (u(\mathbf{x}), v(\mathbf{x}), w(\mathbf{x}))$ is shown on the bottom row. It can be seen, in this bottom row, that in most regions across the section the deformation is restored correctly, although restoration is better achieved in Fig. 4(d).

The mean and median of the deformation error measure the residual nonresolved deformation. They are defined as

$$e_{\mathrm{mean}}(t) = \frac{\sum\limits_{\mathbf{x}\in P} \|\mathbf{U}(\mathbf{x}) - \mathbf{u}(\mathbf{x},t)\|}{\sum\limits_{\mathbf{x}\in P} \|\mathbf{U}(\mathbf{x})\|} \tag{18}$$

and

$$e_{\mathrm{median}}(t) = \frac{\underset{\mathbf{x}\in P}{\mathrm{median}} \|\mathbf{U}(\mathbf{x}) - \mathbf{u}(\mathbf{x},t)\|}{\underset{\mathbf{x}\in P}{\mathrm{median}} \|\mathbf{U}(\mathbf{x})\|} \tag{19}$$

respectively. To evaluate the accuracy of deformation estimation, the mean and median error were computed for 20 sections extracted from the test volume from randomly selected positions $[\alpha_x, \alpha_y, z_0]$. Fig. 5 shows the average $e_{\mathrm{mean}}(t)$ and $e_{\mathrm{median}}(t)$ when using the Vemuri's PDE in (10) and when using the proposed PDE in (16). As can be seen from Fig. 5, when using the NMI-based PDE in (16), the algorithm converged better to the applied deformation. Note that the discontinuity in the graphs reflects a change in the resolution level.

Table II demonstrates the scalability of the developed 2-D to 3-D framework. Obviously, the more resolution levels used, the lower the deformation error. The algorithm running time, when including different levels of resolution, is shown as well (based on implementation using MATLAB and Visual C++ development environment on a WIN/XP OS with 2.0-GHz CPU and with 4-GB RAM).

Both Vemuri's evolution equation and the evolution equation proposed in this study, successfully recover the applied deformation. While the first is computationally less complex, latter allows application to real data scenarios where alignment should be done in the presence of interspecimen variability and comparing images generated by different imaging procedures.

Finally, we demonstrated the IPSM and ICSM algorithms' performance in atlas-guided segmentation of a mouse brain hippocampus. The hippocampal complex, as delineated in the atlas, is shown in Fig. 6. Aligning the atlas and a given celloidin image

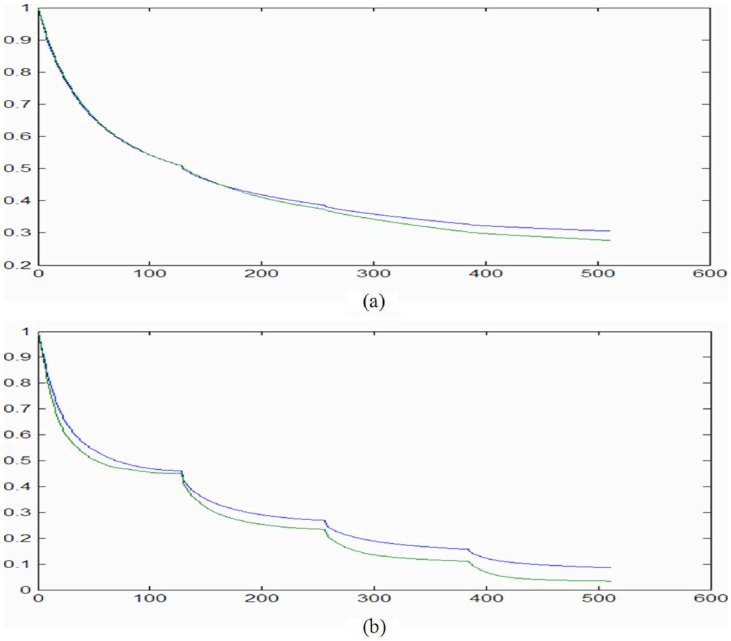

Fig. 5. Average mean (blue) and median (green) error, as defined in (18) and (19), respectively. The results when employing the PDE in (10) and when employing the PDE in (16) are shown in (a) and (b), respectively.

TABLE II
AVERAGE MEAN AND MEDIAN ERROR, AS DEFINED IN (18) AND (19), RESPECTIVELY, ARE SHOWN FOR THE LAST ITERATION OF EACH RESOLUTION LEVEL. THE ALGORITHM RUNNING TIMES ARE ALSO SHOWN, DEMONSTRATING THE TRADEOFF BETWEEN ACCURACY AND COMPLEXITY

	PDE-10			PDE-15		
Resolution level	mean	median	Time (minutes)	mean	median	Time (minutes)
3	0.51	0.51	~0.15	0.46	0.45	~0.75
2	0.39	0.37	~0.7	0.27	0.23	~3.5
1	0.33	0.30	~4.5	0.16	0.11	~15
0	0.31	0.28	~21	0.09	0.03	~65

facilitates an atlas-guided segmentation of structures of interest (the hippocampal structures in this case).

To match a given brain section with a corresponding plane within the atlas, we first employed the IPSM algorithm. This linear alignment stage yielded the segmentation shown on the bottom left part of Fig. 6. Next, we employed the ICSM algorithm to further refine the match between the given brain section and its corresponding image on a curved-surface within the atlas. This nonlinear alignment stage yielded the segmentation shown on the bottom right part of Fig. 6. Comparison of the linear segmentation results with the nonlinear segmentation results shows that the improvement in segmentation accuracy provided by the ICSM algorithm is significant. Specifically, it can be seen that the hippocampus templates (shown in different color shades) after linear mapping from the atlas are positioned somewhat lower and too far to the left than they should be in order to perfectly overlap with the corresponding hippocampus structures in the given celloidin section I_{ms}. Applying the ICSM algorithm improves significantly the overlap between the atlas hippocampal templates and the celloidin image hippocampal structures.

Fig. 7 shows a close-up view of three MBL sections' hippocampus complexes. On the left, the atlas's hippocampal templates were mapped onto the MBL sections employing linear alignment (IPSM algorithm). On the right, the atlas's hippocampal templates were mapped onto the MBL sections

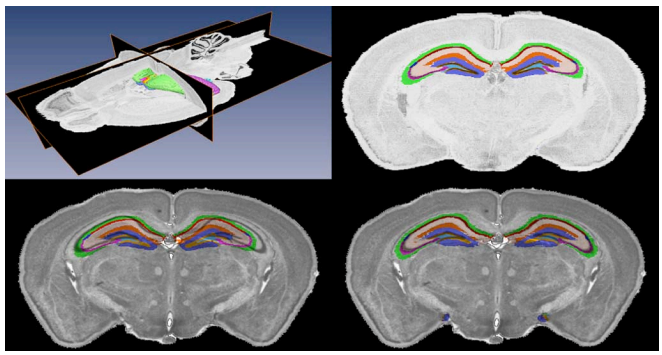

Fig. 6. Cutaway view of the mouse atlas with the regions of the hippocampal formation shown (top left), along with a coronal cross section (top right). The following structures are highlighted: CA1 (red), CA2 (dark blue), CA3 (purple), dentate gyrus (bright blue), granular layer of the dentate gyrus (brown), polymorph layer of the dentate gyrus (cyan), stratum radiatum of the hippocampus (pink), the molecular layer of the dentate gyrus (orange), and the hippocampus oriens layer (green). A coarse atlas-guided segmentation of a section from the MBL database after linear alignment is shown below (bottom left). The image to curved-surface alignment allows for further segmentation refinement (bottom right). Comparing the two alignments on the bottom, it can be seen that the atlas hippocampal templates (top right), after mapping, overlap better the celloidin section hippocampal structures when employing the image to curved-surface alignment (bottom right).

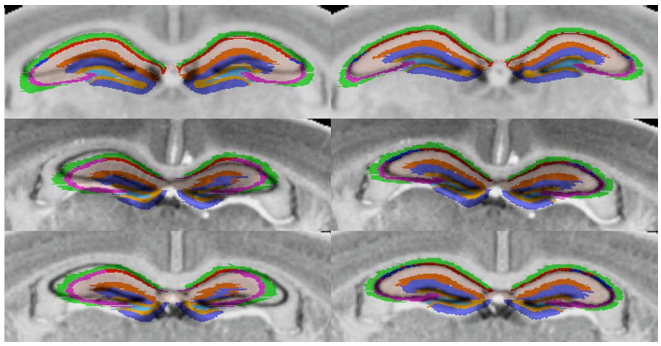

Fig. 7. Atlas-based segmentation of the hippocampus. On the left, the atlas's hippocampal templates were mapped onto the MBL sections employing linear alignment (IPSM algorithm). On the right, the atlas's hippocampal templates were mapped onto the MBL sections employing nonlinear alignment (ICSM algorithm).

employing nonlinear alignment (ICSM algorithm). The improvement in segmentation when applying the nonlinear stage is significant. A quantitative evaluation of this improvement was done as follows. The overlap between the hippocampus segmentation area, provided by an expert (ground truth), and these achieved by the IPSM and ICSM algorithms were computed for 30 randomly selected MBL sections. The mean and standard deviation of the overlap achieved by the ICSM algorithm are 82.86% and 12.90%, respectively. This is significantly better than the mean and standard deviation of the overlap achieved by the IPSM algorithm: 70.61% and 18.86%, respectively. The T test value comparing these two means is 4.728 with a p-value < 0.001.

IV. Conclusion

In this study, we developed an image-based method for section-to-volume image registration. Though the application of our research is on brain mapping, the proposed method is a generic approach for 2-D to 3-D registration. We recovered the deformation field that matched a given brain image with its corresponding image on a curved-surface within the atlas using a level-set formulation and a local normalized mutual information metric.

Employing the algorithm on simulated data validated the proposed approach. Given a brain image, we located its best corresponding image on a plane within the atlas and then restored the deformation field (relative to this plane) that defined a better corresponding image on a curved-surface within the atlas. The efficacy of the proposed algorithm for atlas-guided segmentation was also demonstrated. We successfully achieved fully automated segmentation of the hippocampus structures. This automatic segmentation is especially significant given the labor-demanding task of manual delineation.

As with most image-based registration methods, the proposed approach is limited by imperfect imaging procedure, such as sections with tears or missing parts. Our plan for future study is to explore how prior information, in part available for us by the atlas templates, can be integrated into this method formulation and thereby increase the robustness of this method.

References

[1] I. N. Bankman, *Handbook of Medical Imaging*. San Diego, CA: Academic, 2000.

[2] L. G. Brown, "A survey of image registration techniques," *ACM Comput. Surv.*, vol. 24, pp. 325–376, 1992.

[3] H. Lester and S. R. Arridge, "A survey of hierarchical non-linear medical image registration," *Pattern Recognit.*, vol. 32, pp. 129–149, 1999.

[4] J. B. A. Maintz and M. A. Viergever, "A survey of medical image registration," *Med. Image Anal.*, vol. 2, pp. 1–36, 1998.

[5] J. P. W. Pluim, J. B. A. Maintz, and M. A. Viergever, "Mutual-information-based registration of medical images: A survey," *IEEE Trans. Med. Imag.*, vol. 22, no. 8, pp. 986–1004, Aug. 2003.

[6] A. W. Toga, *Brain Warping*. New York: Academic, 1999.

[7] P. A. Van den Elsen, E. J. D. Pol, and M. A. Viergever, "Medical image matching- A review with classification," *IEEE Eng. Med. Biol. Mag.*, vol. 12, no. 1, pp. 26–39, Mar. 1993.

[8] B. Zitova and J. Flusser, "Image registration methods: A survey," *Image Vis. Comput.*, vol. 21, pp. 977–1000, 2003.

[9] J. H. Hipwell, G. P. Penney, R. A. McLaughlin, K. Rhode, P. Summers, T. C. Cox, J. V. Byrne, J. A. Noble, and D. J. Hawkes, "Intensity-based 2-D-3-D registration of cerebral angiograms," *IEEE Trans. Med. Imag.*, vol. 22, no. 11, pp. 1417–1426, Nov. 2003.

[10] D. B. Russakoff, T. Rohlfing, K. Mori, D. Rueckert, A. Ho, J. R. Adler Jr., and C. R. Maurer, "Fast generation of digitally reconstructed radiographs using attenuation fields with application to 2D-3D image registration," *IEEE Trans. Med. Imag.*, vol. 24, no. 11, pp. 1441–1454, Nov. 2005.

[11] J. Weese, T. Buzug, C. Lorenz, and C. Fassnacht, "An approach to 2D/3D registration of a vertebra in 2D x-ray fluoroscopies with 3D CT images," *Lecture Notes Comput. Sci.*, vol. 1205, pp. 119–128, 1997.

[12] N. Alperin, D. N. Levin, and C. A. Pelizzari, "Retrospective registration of X-ray angiograms with MR-images by using vessels as intrinsic landmarks," *J. Magn. Reson. Imag.*, vol. 4, pp. 139–144, 1994.

[13] H. M. Chan, A. C. S. Chung, S. C. H. Yu, and W. M. Wells, III, "2D-3D vascular regsitration between digital subtraction angiographic (DSA) and magnetic resonance angiographic (MRA) images," presented at the IEEE Int. Symp. Biomedical Imaging: Macro to Nano, 2004.

[14] J. Feldmar, G. Malandain, N. Ayache, S. Fernandezvidal, E. Maurincomme, and Y. Trousset, "Matching 3D MR angiography data and 2D X-rayangiograms," *CVRMed/MRCAS*, 1997.

[15] S. Nicolau, X. Pennec, L. Soler, and N. Ayache, "Evaluation of new 3D/2D registration criterion for liver radio-frequencies guided by augmented reality," *Lecture Notes Comput. Sci.*, 2003.

[16] B. Kim, J. L. Boes, P. H. Bland, T. L. Chenevert, and C. R. Meyer, "Motion correction in fMRI via registration of individual slices into an anatomical volume," *Magn. Reson. Med.*, vol. 41, pp. 964–972, 1999.

[17] A. G. Chandler, T. Netsch, C. A. Cocosco, J. A. Schnabel, and D. J. Hawkes, "Slice-to-volume registration using mutual information between probabilistic image classifications," presented at the Medical Imaging: Image Processing, 2004.

[18] S. Jonic, C. O. S. Sorzano, P. Thevenaz, C. El-Bez, S. De Carlo, and M. Unser, "Spline-based image-to-volume registration for three-dimensional electron microscopy," *Ultramicroscopy*, vol. 103, pp. 303–317, 2005.

[19] W. Birkfellner, M. Figl, J. Kettenbach, J. Hummle, P. Homolka, R. Schernthaner, T. Nau, and H. Bergmann, "Rigid 2D/3D slice-to-volume registration and its application on fluoroscopic CT images," *Med. Phys.*, vol. 34, pp. 246–255, 2007.

[20] T. S. Kim, M. Singh, W. Sungkarat, C. Zarow, and H. Chui, "Automatic registration of postmortem brain slices to MRI reference volume," *IEEE Trans. Nucl. Sci.*, vol. 47, no. 4, pp. 1607–1613, Aug. 2000.

[21] J. Liu, N. Pagoulatos, and Y. Kim, "Ultrasound spatial compounding via registration of 2D slices into 3D volume," presented at the IEEE Int. Ultrasonics, Ferroelectrics, and Frequency Control Joint 50th Anniversary Conf., 2004.

[22] G. D. Rosen, N. T. L. Porte, B. Diechtiareff, C. J. Pung, J. Nissanov, C. Gustafson, L. Bertrand, S. Gefen, Y. Fan, O. J. Tretiak, K. F. Manly, M. R. Park, A. G. Williams, T. Connolly, J. A. Capra, and R. W. Williams, "Informatics center for mouse genomics: The dissection of complex traits of the nervous system," *Neuroinformatics*, vol. 1, pp. 327–342, 2003.

[23] S. Osher and J. Sethian, "Fronts propagating with curvature-dependent speed: Algorithms based on Hamiltons-Jacobi formulations," *J. Comput. Phys.*, vol. 79, pp. 12–49, 1988.

[24] R. Kimmel, *Numerical Geometry of Images*. New York: Springer, 2004.
[25] S. Osher and N. Paragios, *Geometric Level Set Methods*. New York: Springer-Verlag, 2003.
[26] S. J. Osher and P. F. Ronald, *Level Set Methods and Dynamic Implicit Surfaces*. New York: Springer-Verlag, 2003.
[27] B. C. Vemuri, J. Ye, Y. Chen, and C. M. Leonard, "Image registration via level-set motion: Applications to atlas-based segmentation," *Med. Image Anal.*, vol. 7, pp. 1–20, 2003.
[28] G. Hermosillo, C. Chefd'hotel, and O. Faugeras, "Variational methods for multimodal image matching," *Int. J. Comput. Vis.*, vol. 50, pp. 329–343, 2002.
[29] S. Gefen, L. Bertrand, N. Kiryati, and J. Nissanov, "Localization of sections within the brain via 2D to 3D image registration," presented at the IEEE Int. Conf. Acoustics, Speech, and Signal Processing, Philadelphia, PA, 2005.
[30] S. Gefen, N. Kiryati, L. Bertrand, and J. Nissanov, "Planar-to-curved-surface image registration," presented at the Mathematical Methods in Biomedical Image Analysis (MMBIA), New York, 2006.
[31] D. Kozinska, O. J. Tretiak, J. Nissanov, and C. Ozturk, "Multidimentional alignment using the Euclidean distance transform," *Graph. Models Image Process.*, vol. 59, pp. 373–387, 1997.
[32] C. Studholme, D. L. G. Hill, and D. J. Hawkes, "An overlap invariant entropy measure of 3D medical image alignment," *Pattern Recognit.*, vol. 32, pp. 71–86, 1999.
[33] D. H. Wolpert and W. G. MacReady, "No free lunch theorems for optimization," *IEEE Trans. Evol. Comput.*, vol. 1, no. 1, pp. 67–82, Apr. 1997.
[34] D. Whitley, "A genetic algorithm tutorial," Tech. Rep. CS-93–103, Dept. Comput. Sci., Colorado State Univ., Boulder, 1993.
[35] J. Nissanov, L. Bertrand, and O. J. Tretiak, "Cryosectioning distortion reduction using tape support," *Microsc. Res. Tech.*, vol. 53, pp. 239–240, 2001.
[36] P. R. Woods, S. T. Grafton, C. J. Holms, S. R. Cherry, and J. C. Mazziotta, "Automated image registration: I. General methods and intrasubject, intramodality validation," *J. Comput.-Assist. Tomogr.*, vol. 22, pp. 139–152, 1998.
[37] C. Gustafson, O. Tretiak, L. Bertrand, and J. Nissanov, "Design and implementation of software for assembly and browsing of 3D brain atlases," *Comput. Meth. Progr. Biomed.*, vol. 74, pp. 53–61, 2004.
[38] G. D. Rosen, A. G. Williams, J. A. Capra, M. T. Connolly, B. Cruz, L. Lu, D. C. Airey, K. Kulkarni, and R. W. Williams, "The mouse brain library @ www.mbl.org," presented at the Int. Mouse Genome Conf., 2000.
[39] P. A. Burt and E. H. Adelson, "The Laplacian pyramid as a compact image code," *IEEE Trans. Commun.*, vol. 31, no. 4, pp. 532–540, Apr. 1983.
[40] N. M. Alpret, J. F. Bradshaw, D. Kennedy, and J. A. Correia, "The principal axes transformation—A method for image registration," *J. Nucl. Med.*, vol. 31, pp. 1717–1722, 1990.
[41] F. L. Bookstein, "Principal warps: Thin-plate splines and the decomposition of deformations," *IEEE Trans. Pattern Anal. Mach. Intell.*, vol. 11, no. 6, pp. 567–585, Jun. 1989.

Smadar Gefen (M'96) received the B.Sc. and M.Sc. degrees in electrical engineering from Tel-Aviv University, Tel-Aviv, Israel, in 1993, and the Ph.D. degree in electrical and computer engineering from Drexel University, Philadelphia, PA, in 2002.

Since 1993, she has been involved in research and development in the field of image processing. From 1995 to 1997, she was a Senior Engineer with Iterated Systems, Atlanta, GA, working on image and video compression, and from 1997 to 1998, she was an Associate Member of the Media Vision Group at Sarnoff Corporation working on image registration. While conducting the study described in this paper, she was with the Laboratory for Bioimaging and Anatomical Informatics, Department of Neurobiology and Anatomy, Drexel University College of Medicine. Currently, she is with PVI Virtual Media Services LLC, Lawrenceville, NJ. Her research interests focus on image and video processing including tracking, registration, and classification.

Nahum Kiryati (SM'95) received the B.Sc. degree in electrical engineering and the post-B.A. degree in the humanities from Tel-Aviv University, Tel-Aviv, Israel, in 1980 and 1986, respectively, and the M.Sc.and D.Sc. degrees from The Technion—Israel Institute of Technology, Haifa, in 1988 and 1991, respectively.

He was with the Image Science Laboratory, ETH-Zurich, Switzerland, and with the Department of Electrical Engineering, The Technion. He is currently with the School of Electrical Engineering, Tel-Aviv University. His research interests are in image analysis, computer vision and medical imaging.

Jonathan Nissanov (M'96) received a B.A. degree in molecular biology and the Ph.D. degree in biology from the University of Colorado, Boulder, in 1979 and 1987, respectively.

He was an National Institutes of Health Postdoctoral Fellow from 1987 to 1989 at the Neurobiology Unit, University of California, San Diego. After serving as a Research Associate (1989–1992) in the Department of Electrical and Computer Engineering, Drexel University, Philadelphia, PA, he joined the School of Biomedical Engineering, Science and Health Systems, Drexel University. Since 2000, he has been an Associate Professor in the Department of Neurobiology and Anatomy, Drexel University. His research interests are bioimaging, image analysis, and neuroinformatics.